Title
A methodology to compute the critical current limit in Nb3Sn magnets

Journal
Superconductor Science and Technology, 34(2)

ISSN
0953-2048

Authors
Vallone, G
Anderssen, E
Bordini, B
et al.

Publication Date
2021-02-01

DOI
10.1088/1361-6668/abc56b

Peer reviewed

A Methodology to Compute the Critical Current Limit in Nb_3Sn Magnets

G. Vallone, E. Anderssen, B. Bordini, P. Ferracin, J.F. Troitino, S. Prestemon

***Abstract*—Numerous experiments have shown that the loads applied to Nb_3Sn strands and cables can reduce their critical current. Experiments, performed on uniaxially loaded strands, allowed to define clear laws to describe the evolution of the critical surface as a function of the applied current, field, temperature and strain. It is, however, still unclear how these laws can be applied to superconducting magnets. The present paper proposes a methodology to estimate the critical current and temperature margin reduction on superconducting magnets due to stress on the superconducting material. The methodology is tested on the MQXF magnets, a quadrupole developed for the High Luminosity LHC project, and successfully validated by comparing computed strain with data from strain gauge measurements. Results suggested that, because of the stresses arising in winding during assembly, cool-down and powering, the current limit of the magnet is lower than the expected short sample limit, and that the most critical region does not coincide with the peak field location.**

***Index Terms*—Nb_3Sn, Rutherford Cables, Transversal Pressure, Critical Current, Scaling Law, Superconducting Magnet, Quadrupole**

I. Introduction

SUPERCONDUCTING magnets are characterized by a critical current, defined as the maximum current that the magnet can reach without crossing the critical surface at any point in the superconducting coils. Nb_3Sn magnets are generally operated either at 4.2 K or in superfluid helium at 1.9 K. Their limit current is usually obtained starting from measurements of the critical current on strands extracted from the cables used in the coils of the same magnet. These strands are generally referred to as short-samples, and the related current limit is the so-called short sample limit. To ensure that the samples performances are representative of the coil ones, they undergo heat treatment with the corresponding magnet coils. The samples critical surface can be parametrized, for example with the approach described in [1]. This allows to extract the critical field as a function of the current at the operating temperature [2].

It was shown in the past by numerous experiments that the Nb_3Sn superconducting critical surface is a function of not only of the temperature, magnetic field and current density, but also of the applied strain state [3]–[10]. In particular, the applied strain can cause a reversible critical current reduction, that disappears when the strain is removed, and an irreversible critical current reduction (degradation), due to the mechanical failure of the superconducting elements [8], [11].

In the operative conditions, superconducting coils can be subject to tridimensional strain states, caused by the e.m. forces and by the prestress, applied in order to limit motions during powering. These forces can generate significant strain/stresses in the conductor [12]. As a consequence, the conductor critical surface can move, reducing the available margin or quenching prematurely the magnet. In other words, the actual limit current for the magnet might be different from the one computed from the short sample measurements. In order to avoid this, it is crucial to define a clear limit criteria for correctly designing these magnets, especially in view of the continuously growing magnet fields and e.m. forces required by particle accelerators [13].

Nowadays, most magnets are designed considering an empirical criteria defined on the basis of the experience from previously tested magnets, which states that, in order to avoid or minimize conductor degradation, the equivalent stress inside the coil has to be lower than 150-200 MPa [12]. As the direct measurement of the strain with strain gauges on the coil is considered unreliable [14], this stress is generally extracted from validated FE models. These numerical models generally represent the coil as a block of an equivalent uniform material, assumed orthotropic in 2D models and isotropic in 3D models, because of difficulties in defining the correct reference system in the latter case. More refined approaches were used in some cases, as for example modeling the single cables [15], or separating the cable from the insulation [16]. Recently, a coil model at the strand level, with geometry extracted from a coil cross section picture, has been proposed in [17]. A cable and coil modeling strategy at the strand level was proposed in [18], and used to predict the mechanical stiffness of the coil and its dependence on the mechanical properties of the various components. These more complex representations, however, cannot be easily linked to the empiric criteria mentioned above.

On the other hand, it is relatively easy to test longitudinally stretched Nb_3Sn strands. This allowed to define clear laws in the reversible region [9]. A number of works tried to express the critical current evolution as a function of the three-dimensional strain state, as for example in [19]–[21]. In [22], a model was proposed to estimate the 3D strain state inside a conductor under tensile stress. In [9], an exponential scaling law was proposed. This law was applied to match the critical current as measured on superconducting strands

Automatically generated dates of receipt and acceptance will be placed here
This work was supported by the High Luminosity LHC Project at CERN and by the DOE through the U.S. Magnet Development Program.

G. Vallone, E. Anderssen, P. Ferracin and S. Prestemon are with Lawrence Berkeley National Laboratory, Berkeley, CA 94720 USA (e-mail: gvallone@lbl.gov).

B. Bordini and J.F. Troitino are with the European Organization for Nuclear Research (CERN), 1211 Geneva, Switzerland.

Colour versions of one or more of the figures in this paper are available online at https://iopscience.iop.org.

Digital Object Identifier: xx

under transversal pressure in [23]. This result, and the intrinsic tridimensionality of the exponential scaling law, suggested that this approach may be apt at reproducing the current reduction in strands under a tridimensional strain state, as is the case for the ones in superconducting coils. In [24], we showed how the law can be applied to match the critical current reduction on Rutherford cable stacks. Experimental results and the procedure are reported in [25], [26]. New tests were performed, showing similar performances on Rutherford Cable based on $1\,\mathrm{mm}$ RRP wires [27]. Similar experiments were performed on two different set-ups, one in Twente [5] and one at NHMFL [28].

In this paper we extend the same methodology, applied in [24] to a stack of cables, to a full coil of a superconducting magnet, with the goal of estimating the reduction of magnet critical current due to strain in the superconductor, in the reversible region. As a benchmark, the approach was used to build a 2D FE magneto-mechanical model of a superconducting quadrupole and to obtain the impact of mechanical loads on its critical current limit and temperature margin.

The paper is organized as follows: in Section II, we describe the methodology listing the necessary steps and the fundamental equations; in Section III, we introduce the MQXF magnet and a FE model built using the presented methodology; in Section IV, the model is validated on top of the available measurements; in Section V, we present the strain and stresses as computed on the superconducting strands; in Section VI, we compute the critical current, the critical field and the temperature margin; in Section VII we study how the critical current reduction obtained with this methodology compares to the stresses as computed on a simplified FE model with smeared coil properties.

II. Methodology Description

The current limit of superconducting magnets for particle accelerators is usually estimated finding the current at which the peak field on the coil crosses the critical surface, measured with an strand extracted from the magnet cable, and mounted on a barrel. Therefore this approach, traditionally adopted so far, neglects the impact on the critical surface of the strain applied on the strands. Also, it is worth noticing that in a magnet this strain changes continuously as a function of the current, because of the variation of the applied e.m. forces. Here we propose to take into account this effect to refine the limit accuracy. In order to do this, one needs: an estimate of the magnetic field on a strand; an approach to estimate the strain applied on the superconducting region of the strands, as a function of the applied current; and a method to update from these strains the critical surface. One has to perform this computations on each strand, in fact, because of the influence of the strain on the critical surface, the critical point can now be in any region of the superconducting coils, and not always at the peak field location.

The methodology proposed here is made of a sequence of steps:

1) Create an electromagnetic and a mechanical model with a separate representation of the superconducting regions

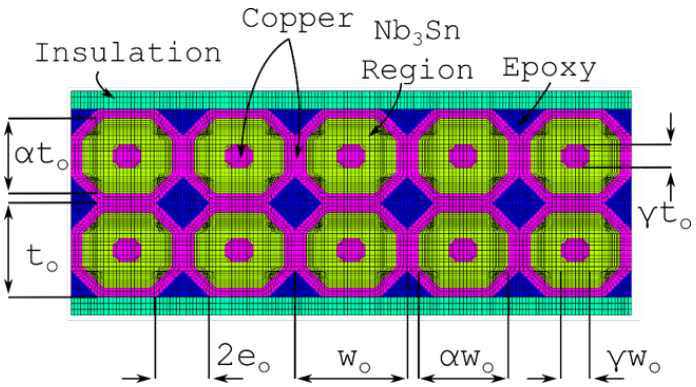

Fig. 1. Representative FE geometry and mesh used to model a single cable at the strand level [24].

TABLE I
Material Properties

Parameter	Unit	Value
Copper Elastic Modulus (R.T.)	GPa	110
Copper Elastic Modulus (4.3 K)	GPa	120
Copper Yield Strength	MPa	40
Copper Tangent Modulus	GPa	5
Nb_3Sn Region Elastic Modulus (R.T.)	GPa	100
Nb_3Sn Region Elastic Modulus (4.3 K)	GPa	70
Epoxy Resin Elastic Modulus	GPa	5
Impregnated Insulation Elastic Modulus (R.T.)	GPa	13
Impregnated Insulation Elastic Modulus (4.3 K)	GPa	20
Copper Thermal Contraction	mm/m	3.3
Epoxy Thermal Contraction	mm/m	11.9
Impregnated Insulation Thermal Contraction	mm/m	7.49
Nb_3Sn Thermal Contraction (α_{Nb_3Sn})	mm/m	1.8
Nb_3Sn Region Thermal Contraction (α_g)	mm/m	2.5

2) Compute the current/field transfer function for all the superconducting regions
3) Extract the strain on every superconducting region as a function of the powering current
4) Compute the critical current for each strand using the exponential scaling law
5) Find the minimum powering current for which the critical current is crossed at any strand.

The knowledge of the strain function as a function of the applied current can then be used also to extract the updated critical field and temperature margin. The most critical steps in the procedure are the coil modelling strategy (point 1), the computation of the strain function (point 3), and the computation of the critical current for each strand (point 4). These steps are also general and can be applied to any magnet whose windings are made of Rutherford cables.

A. Coil Modeling Strategy

Each Rutherford cable composing the coil can be modelled, as suggested in [24], by representing each strand as three concentric octagons: the central part of the copper matrix, then a Nb_3Sn region, comprising the non-copper material and a portion of the copper matrix, and finally the outer ring of the copper matrix. The bare cable is wrapped in G10 insulation and the voids are filled with epoxy. The geometry of the cable is shown in Figure 1. The various components

are considered bonded because of the impregnation process and share the nodes across their contours. The outer copper octagon thickness t_0 is assumed to be equal to half of the bare cable thickness t_c. If w_c is the reacted cable width, and N_s the number of strands, the width of the octagons has to be equal to $2w_c/N_s$. Indicating with A_c is the cable cross-sectional area, with d_s the strand diameter, with β_t the cable twist angle, the width of the epoxy gaps $2e_0$ can be computed as [24]:

$$e_o = \sqrt{\frac{t_o w_o - A_c \eta_f / N_s}{2}} \tag{1}$$

where η_f is the filling factor, defined as [29]:

$$\eta_f = \frac{N_s \pi (d_s/2)^2}{A_c \cos \beta_t} \tag{2}$$

The inner octagons are scaled from the outer ones, keeping the same thickness/width ratio. We can then define two scaling parameters: α for the Nb_3Sn octagon and γ for the inner copper region. The thickness and width of the Nb_3Sn octagon are equal to αt_o and αw_o; the ones of the inner copper region are instead γt_o and γw_o. The scaling parameters can easily be estimated by measuring the areas of the different regions on a microscope image of the considered strand.

The material properties used are listed in Table I. The following equation was used to estimate α_g, the contraction of the Nb_3Sn region:

$$\alpha_g = \rho_{Nb_3Sn}\ \alpha_{Nb_3Sn}\ + \rho_{Cu}\alpha_{Cu} \tag{3}$$

where the ρ symbol is used for the volume fraction, α for the thermal contraction and the subscripts Nb_3Sn and Cu indicate respectively the superconducting and non-superconducting material inside the superconducting region.

Each cable has then to be positioned within the coil: this is trivial for block configurations but requires a set of assumptions for a cosθ magnet. The approach used hereafter is described in Appendix A. Hereafter, we refer to the models created with this approach as *FE strand model*, while the traditional representations using smeared properties within the coil will be indicated as *FE block model*.

B. Strain Function Computation

The main parameter governing the critical current reduction in the reversible region is the strain function $s(\boldsymbol{\varepsilon})$, defined as:

$$s(\boldsymbol{\varepsilon}) \equiv \frac{B_{c2}(0, \boldsymbol{\varepsilon})}{B_{c2}(0,0)} \tag{4}$$

where $\boldsymbol{\varepsilon}$ is the strain tensor and $B_{c2}(T, \boldsymbol{\varepsilon})$ is used to indicate the upper critical field as a function of strain and temperature.

The impact of the strain function on the pinning force can be expressed as [9]:

$$F_p = J_c(B, T, \boldsymbol{\varepsilon}) \times B = C g(s(\boldsymbol{\varepsilon})) h(t) b^p (1-b)^q \tag{5}$$

where b is the reduced field and t the reduced temperature, defined as a function of the critical temperature $T_c(\varepsilon)$ and critical field B_{c2} as follows [9]:

$$T_c(\boldsymbol{\varepsilon}) = T_c(0) s(\boldsymbol{\varepsilon})^{\frac{1}{w}} \qquad t = T/T_c(\boldsymbol{\varepsilon}) \tag{6}$$

$$B_{c2}(T, \boldsymbol{\varepsilon}) = B_{c2}(0,0) s(\boldsymbol{\varepsilon})(1 - t^{\nu}) \qquad b = B/B_{c2}(T, \boldsymbol{\varepsilon}) \tag{7}$$

The parameter w is the cross link parameter, empirically found to be equal to 3. ν is the upper critical field parameter, equal to 1.5 on a wide range of strain. This value is close to the one calculated with the Werthamer theory. The parameters p and q are the pinning force shape parameters, which depend on the pinning mechanism and here are assumed to be equal to 0.5 and 2. The function $g(\boldsymbol{\varepsilon})$ is equal to $s(\boldsymbol{\varepsilon})^{e_s}$, where e_s is a parameter generally assumed to be 1.0 or 1.1.

To compute the strain function we use the exponential scaling law [9]:

$$s(\boldsymbol{\varepsilon}) = \frac{e^{-C_1 \frac{J_2+3}{J_2+1} J_2} + e^{-C_1 \frac{I_1^2+3}{I_1^2+1} I_1^2}}{2} \tag{8}$$

where C_1 is a constant depending on the particular strand used, and can be derived from critical current measurements performed on uniaxially loaded strands; I_1 is the first invariant of the strain tensor and J_2 is the second invariant of its deviatoric part, that can be expressed as a function of the principal strains ε_1, ε_2 and ε_3:

$$I_1 = (\varepsilon_1 + \varepsilon_2 + \varepsilon_3) \tag{9}$$

$$J_2 = \frac{1}{6}\left[(\varepsilon_1 - \varepsilon_2)^2 + (\varepsilon_2 - \varepsilon_3)^2 + (\varepsilon_3 - \varepsilon_1)^2\right] \tag{10}$$

In Eq. 9, the strain components are extracted from the total strain tensor $\boldsymbol{\varepsilon}$, considered to be the sum of the mechanical strain tensor $\boldsymbol{\varepsilon}_M$ and the residual strain $\boldsymbol{\varepsilon}_T$, due to the differential thermal contraction of the copper and Nb_3Sn during the cool-down from reaction temperature. It was shown in [9] that the longitudinal component of $\boldsymbol{\varepsilon}_T$ is a constant (ε_{l0}), function of the strand design, and that the transversal components ε_{t0} can be expressed as [9]:

$$\varepsilon_{t0} = -\nu \varepsilon_{l0} + K \tag{11}$$

where ν is the Poisson ratio and K a fitting parameter equal to 0.1.

The Rutherford cable modeling strategy proposed allows to extract the strain state in the superconducting region of the cable. In [24], the same authors showed that the methodology could match the critical current reduction as measured on Rutherford cable stacks [26]. To achieve this correlation with the experimental data, it was necessary to amplify the transversal strain components of $\boldsymbol{\varepsilon}_M$ in the Nb_3Sn area with a factor α_f:

$$\overline{\varepsilon_t} = \alpha_f \varepsilon_t \tag{12}$$

where ε_t is the transversal strain, and $\overline{\varepsilon_t}$ the amplified transversal strain. The parameter α_f was calibrated on the available experimental data [26] and found equal to 2.

C. Critical Current Computation

The critical current on the strand can be computed as follows:

$$I_\mu(\theta) = \frac{1}{A_s} \int_A I_c(s(\varepsilon(x,y)), B(x,y), T(x,y) dA \tag{13}$$

where A_s is the strand superconducting area, I_c the critical current, (x, y) the coordinates of a generic point in

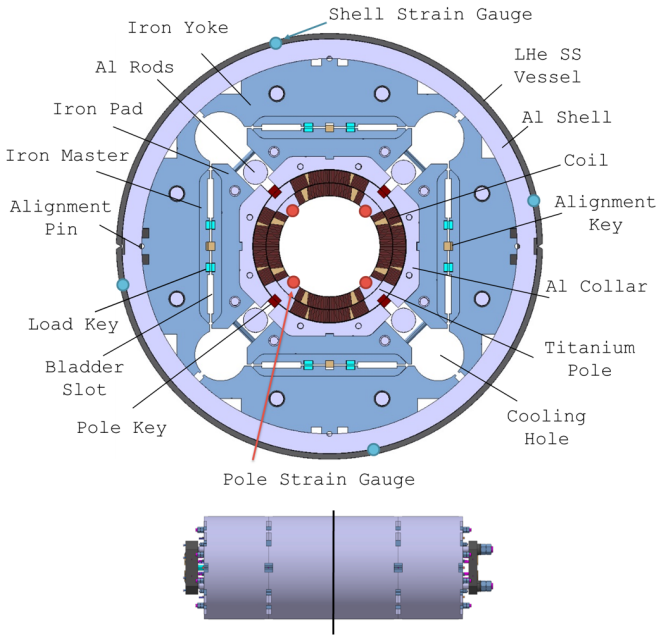

Fig. 2. MQXF cross-section (top), and longitudinal view of the short models (bottom). The strain gauges were installed on the shell and the winding poles, as shown by the circular markers. The vertical line in the bottom view provides their longitudinal position.

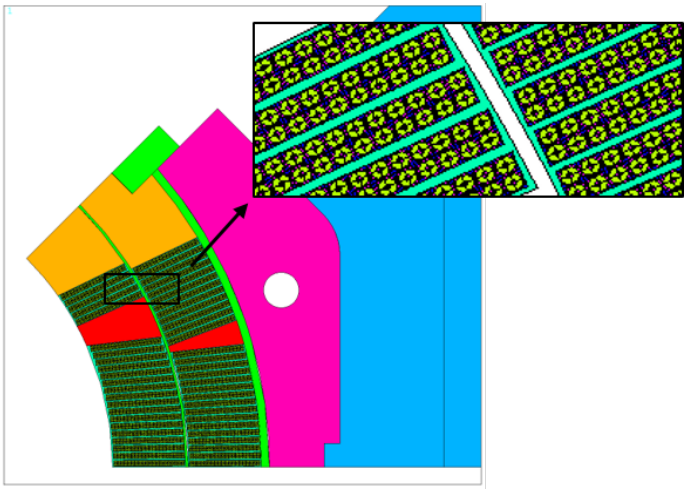

Fig. 3. MQXF FE strand model geometry. The cable geometry is magnified to show the actual geometry of the strands and cables. The keystone angle is not included in the actual cable geometry but only in the insulation.

the superconducting region. This approach assumes a perfect current redistribution within the strand, and is applied here for its relative simplicity. Using these assumptions, the critical current computation can match with very good accuracy the available experimental data on Rutherford cable stacks [24], [26].

III. MQXF Strand Model

The Nb_3Sn quadrupole MQXF is part of the High-Luminosity upgrade [30], and will be installed in the LHC triplets. The magnet aims to an ultimate gradient of $143.2\,\mathrm{T/m}$ in a $150\,\mathrm{mm}$ aperture, at an ultimate current of $17.89\,\mathrm{kA}$ [2].

TABLE II
Cable parameters

Parameter	Unit	Value
Strand	/	RRP 108/127
Strand diameter	mm	0.85
Number of strands in cable	/	40
Copper to non-copper	/	1.2
Cable Bare Width	mm	18.15
Mid Thickness	mm	1.525
Keystone Angle	degrees	0.40
G10 Insulation Thickness	mm	0.145

The MQXF design allows to apply a controlled azimuthal prestress at room temperature by means of the bladder and key technology [31]. The longitudinal prestress is instead provided by longitudinal rods, pretensioned by means of an hydraulic piston and locked in this deformed state with bolts. The differential thermal contraction of the various components increases both the azimuthal and longitudinal prestress during the magnet cooldown at cryogenic temperature. A more detailed description of the magnet mechanics can be found in [32]–[36].

Many 1.5 m long models (*short models*) and full length magnets were tested. Four of them reached the target current of $17.89\,\mathrm{kA}$. The others were limited by what was considered to be mechanical or electrical defects [37]–[39]. The short sample limit of all these magnets varied between $21\,\mathrm{kA}$ and $21.5\,\mathrm{kA}$.

For all the short models, the mechanical performance of the structure was monitored during assembly, cooldown and powering by means of electrical strain gauges, installed on the aluminum shells and on the winding poles [33]. The strain gauge locations are shown in Figure 2: four gauge locations were used on the shell, and every coil had gauge installed on the winding pole. On all these locations two gauges were installed: one, measuring the azimuthal strain, and one, measuring the longitudinal strain. This allows, knowing the material elastic modulus, to extract the local azimuthal and longitudinal stresses.

Different prestress levels were applied to various magnets. For the azimuthal prestress, two different levels can be considered: the MQXFS1 level, with an azimuthal winding pole stress at cold of $80\,\mathrm{MPa}$; and the MQXFS4 level at $106\,\mathrm{MPa}$. These two models are used in the following sections as reference for the mechanical performances of the magnet. They both reached a maximum current higher than the target of $17.89\,\mathrm{kA}$. MQXFS1 was limited at 94% of the short sample limit. For the short model MQXFS4, the magnet training was not completed. As a consequence, it was not possible to verify if the actual short sample limit could be reached or not. In both magnets (and also on all the other models tested so far), the coil detached from the winding pole during powering.

A. Geometry and Mesh

The FE models were coded in ANSYS APDL. The geometry was defined assuming that the cables are distributed evenly inside each conductor block. The keystone angle is neglected in the cable geometry, and the contribution is instead

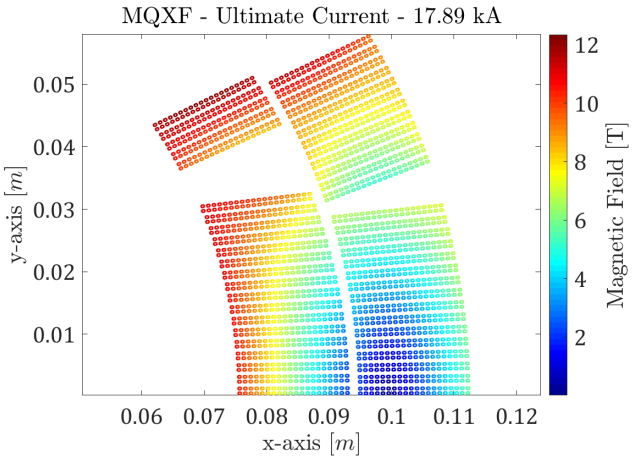

Fig. 4. Magnetic field computed with the strand model. The model results are in close agreement from the ones computed in other softwares, e.g. Roxie [2].

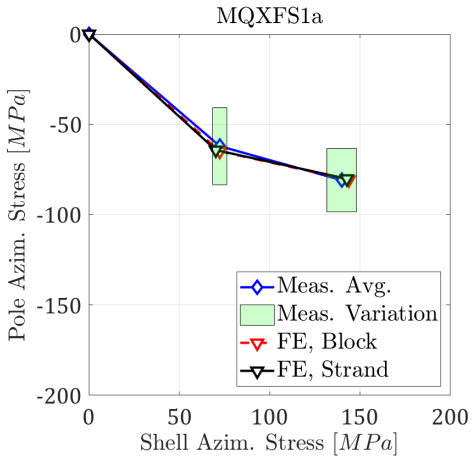

Fig. 5. Transfer Function of MQXFS1a, the first short model quadrupole tested. The points show the shell and coil stresses as measured and computed after loading and cool-down. Remarkable agreement is found between the cable model and the measurements, with results in line with the ones from the coil block FE model.

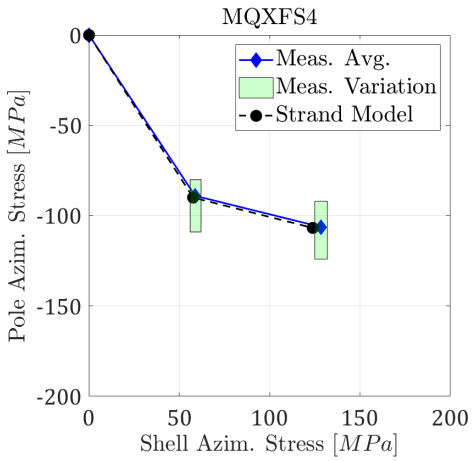

Fig. 6. Mechanical transfer function of MQXFS4.

introduced by varying the local insulation thickness. The centroid of each cable is assumed to stay at the mid-radius of the block. The mathematical formulation of the cable position is provided in Appendix A. The cable and strand parameters are provided in Table II. The resulting geometry and mesh are showed in Fig. 3.

All the coil components (strands, epoxy, insulation) shared the nodes across the boundaries, simulating a glued condition. The coil blocks are then glued to the wedges. As the coils are impregnated, the glued assumption is reasonable. In principle, the impregnation also bonds the coils to the winding poles. However, this bonding is known to often fail during the life cycle of the magnets. In general, damage can be seen on tested coils around the interface between the coils and the winding poles. Measurements and models show that, when a low preload is applied to the magnet, this interface break progressively until a complete separation is created between the coil and the pole [34].

The contact were defined after the approach described in [34]. In this work it was shown that the progressive detachment of the coil from the winding poles can be simulated by introducing cohesive elements at the interface. However, it was also shown that for the MQXFS1 magnet this interface was completely broken after few training quenches. This means that, if we want to simulate the ideal limit of this magnet, it is possible to remove the cohesive material definition from the contacts, and to allow the separation of standard contact elements from the very start of the simulation. The real debonding is probably happening between the strands closer to the pole and the epoxy and insulation bonded to the pole [34]. Here, for simplicity, the debonding is instead introduced at the pole/insulation interface. Sliding contacts allow for the relative displacements of the inner and outer layer.

IV. Strand Model Validation

A. Magnetic results

The e.m. forces and the magnetic field were computed using the geometry shown in Figure 3. The mesh is the same as the one used for the mechanical model, with the addition of air elements in the void spaces between parts. The nodes at the interfaces between the parts were coupled. The computed magnetic field on the strands is shown in Fig. 4. At nominal current, the peak field on the conductor is equal to 11.36 T. The difference between this result and the available measurements is less than 1%. It is worth noticing that the result is in agreement also with the reference simulation for the MQXF magnet [2].

B. Mechanical Results - Preload and Cool-Down

The mechanical status of the MQXF magnet are usually summarized by looking at the transfer function between the shell azimuthal stress and the pole azimuthal stress, shown in Fig. 5. In this plot, the three points of each line depict the status of the magnet before loading, after loading at room temperature, and after cool-down. Two lines represent the FE model results, as obtained from the model described in this paper and a more traditional model representing the coil as blocks of uniform materials. Another line represents the

experimental measurements, performed with the strain gauges installed on the locations shown in Fig. 2. Finally, the green squares represent the measured variation of the stresses on the four measuring locations on the shell and on the winding poles.

The results are shown for the first tested magnet, MQXFS1 [40], in Fig. 5. Another validation is provided at the load level of the MQXFS4 magnet, as shown in Fig. 6. The strand model results are very close to the measured values. The result is particularly impressive if we consider that no calibration was needed to reach this agreement. It can be seen that the computed stresses are also very close to the one from the FE block model. However, this result was obtained in the past via a calibration that brought the coil elastic modulus to 20 GPa [33].

This agreement between the numerical model and the measurements suggests that the modeling methodology is able to predict with very good accuracy the stiffness and the thermal contraction of the winding in both the transversal and radial direction. The result is another good verification of the performances of the approach used to model cables. This model would have in fact allowed to predict the cable mechanics without the use of fitting parameters. As different stiffness are produced by different cable designs and insulation schemes, the approach would allow in future to predict the mechanical behavior of the magnets without relying on the results from past models or measurements on cable stacks in different arrangements.

C. Coil Thermal Contraction

Given the good agreement with the measurements after cooldown, it is interesting to understand what is the equivalent integral thermal contraction obtained with this modeling strategy. Present analysis of the MQXF magnet use a thermal contraction value estimated with a parametric analysis, described in [33]. The value found to match the stress level in the magnet after cool-down was equal to $3.9\,\mathrm{mm/m}$ in the coil. This is significantly higher than the one used in the past, $3.3\,\mathrm{mm/m}$. This parameter allowed for a remarkable agreement between the numerical models and the measurements performed on many MQXF magnets.

The thermal contraction can be evaluated by modeling an unloaded and unconstrained 10-stack and cooling it down to cryogenic temperature. The total contraction obtained with this methodology is equal to $4.03\,\mathrm{mm/m}$, very close to the one obtained by the optimization.

However, this might not be the best estimate of the actual thermal contraction in operative conditions. In this case, in fact, the copper is most likely in a plastic state, and its modulus is lower. In an experimental set-up, this would mean that, as some authors observed in the past, '*the measurement of the thermal-contraction integral at zero stress is not very meaningful*' [41], [42]. If we consider instead the copper as already in a plastic state, the total deformation from the model is equal to $4.2\,\mathrm{mm/m}$.

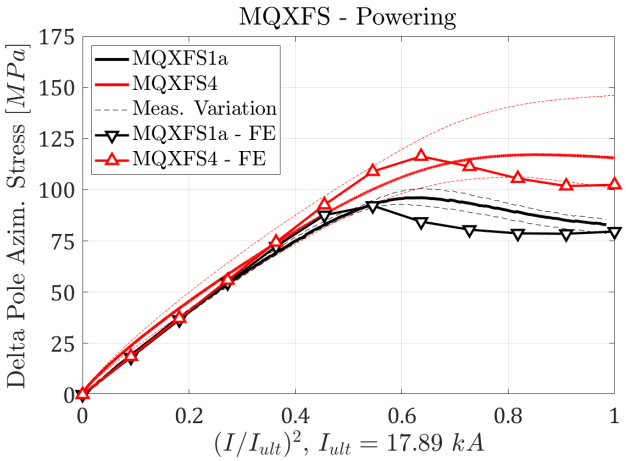

Fig. 7. Stress as measured on the pole during powering of MQXFS1a and MQXFS4, and as computed with the FE model. The measurement variation shows the maximum and minimum measured values across the four quadrants of the magnets.

D. Mechanical Results - Powering

The model was finally used to simulate the mechanical behavior during the magnet powering. The computed winding pole azimuthal stress, at the strain gauge locations, is shown in Fig. 7 as a function of the squared current, proportional to the applied e.m. forces. The results are shown for the MQXFS1 and MQXFS4 magnets, along with the measured pole stress average and its variation across the four quadrants. The azimuthal stress, initially negative thanks to the applied prestress, gradually increases because of the e.m. forces. The change in slope of the curve is generally considered an indication of the detachment of the coil from the pole. The magnet powering is substantially divided in two phases: a first linear phase, when the coil pole block is still in contact with the winding pole, and a second phase when it detaches. The plot in Fig. 7 shows that this detachment is gradual. In other magnets, as for example TQ [43], the behavior was much more linear in the two phases.

The slope of the linear phase is similar for the two magnets and in perfect agreement with the FE model results. The gradual detachment, and the different behavior between the two magnets, is also well predicted by the FE model. The maximum difference between the measured and computed values is equal to 15 MPa.

V. Stress and Strain in the Strands

For the following analysis we consider as a reference the short model MQXFS4 [39], considered the best performing magnet until now, that showed unloading. As the coil is detached from the pole, the strain conditions during powering in this magnet should be equivalent to the ones of the other tested magnets, as for example MQXFS1. However, the amount of plastic strain cumulated in the copper matrix will vary as a function of the applied prestress even when the magnet is unloaded. Therefore, in the Nb_3Sn region some elastic strain can build-up to react the deformation of the copper.

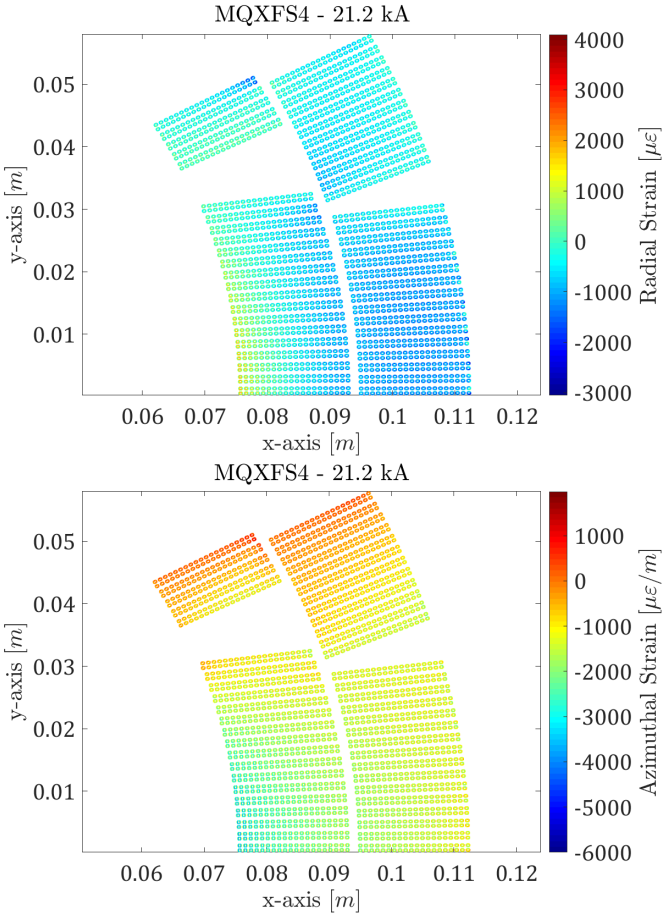

Fig. 8. Radial (top) and Azimuthal (bot) strain on the Nb_3Sn regions of the strands at short sample current for the MQXFS4 magnet.

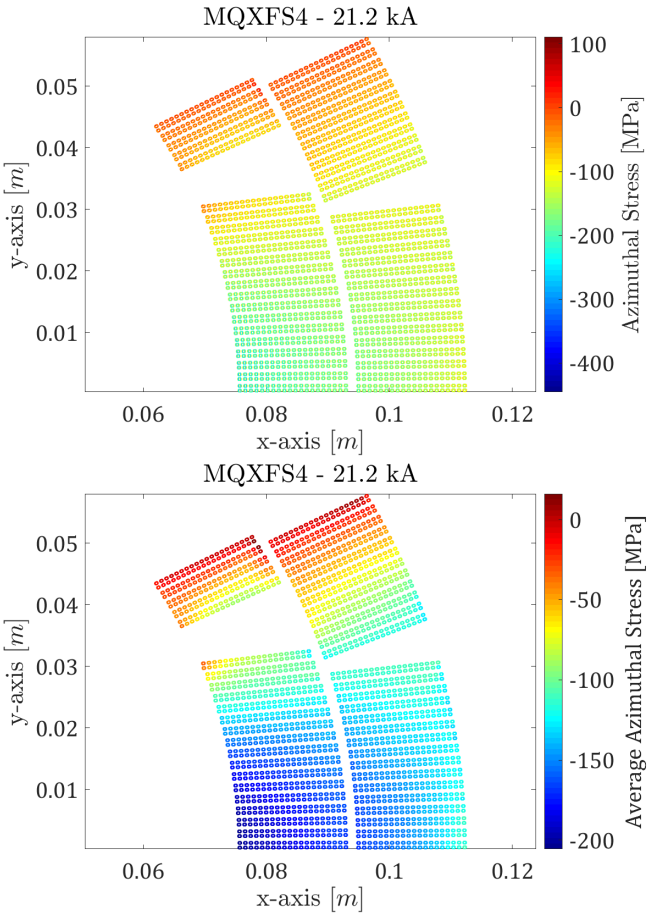

Fig. 9. Azimuthal stress on the Nb_3Sn regions of the strands at short sample current for the MQXFS4 magnet, non-averaged (top) or averaged (bot) over each strand.

The radial and azimuthal strain contours at short sample current are shown in Fig. 8. The azimuthal strain shows mostly compression, with a maximum of 3000 $\mu\varepsilon$ and a lower amount of tension on the pole turn of 1000 $\mu\varepsilon$. The radial strain varies instead from -3000 $\mu\varepsilon$ to 4000 $\mu\varepsilon$. The azimuthal stress in the same condition is instead provided in Fig. 9 (top). The minimum stress is on the inner strand of the last turn (on the mid plane) and equal to -445 MPa. Fig. 9 also provides the azimuthal stress but averaged on each strand. The minimum stress is again on the same strand, with an average of -205 MPa.

VI. Critical Current Computation

A. Strain Function

The average strain function on each strand, at short sample current, is shown in Fig. 10. The result is not directly applicable to estimate the critical current (Eq. 13 should be used instead), but provides a meaningful indication of the strain impact on the various region of the magnet. The lowest value is equal to 0.8, for a strand located on the mid-plane. The pole turn shows a slight increase of the strain function from the unloaded value of 0.93. This is due to the residual strains created during loading and cool-down. Finally, a decrease of the strain function is also seen in the second turn of the pole

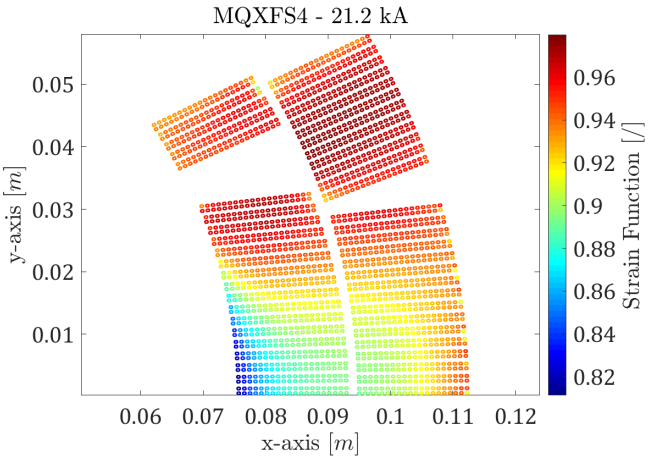

Fig. 10. Strain function computed at the short sample current for the MQXFS4 magnet and averaged on each strand. T = 1.9 K.

block of the inner layer. In this region, the e.m. forces push the cable against the corner of the outer layer pole block, creating a stress amplification region.

In this study, the current reduction due to strains in the radial and azimuthal direction are considered equal. This is coherent with the exponential strain function formulation. In

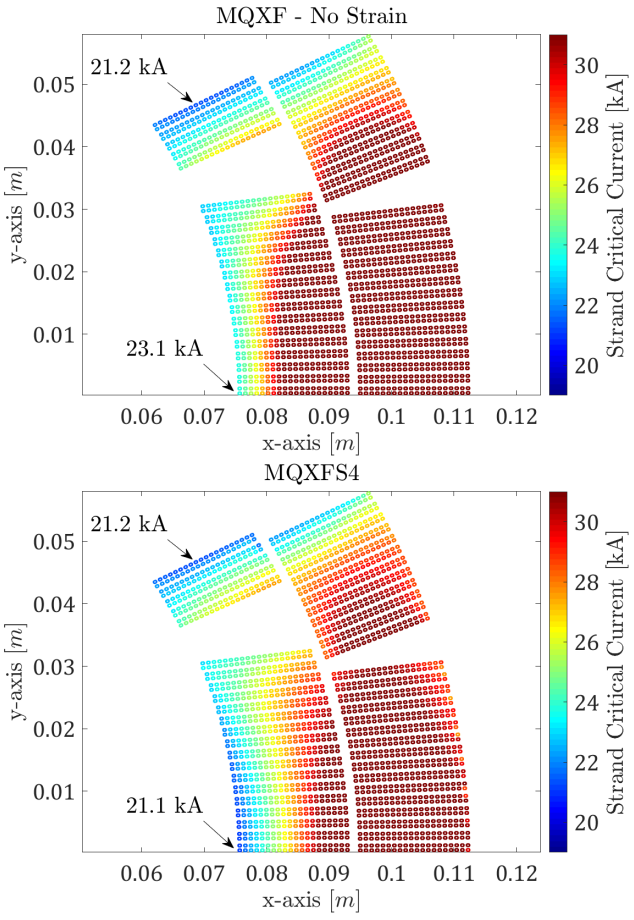

Fig. 11. Critical current for each strand when considering the strands at short sample limit (top), and introducing the actual strain function computed by the FE strand model (bottom). T = 1.9 K.

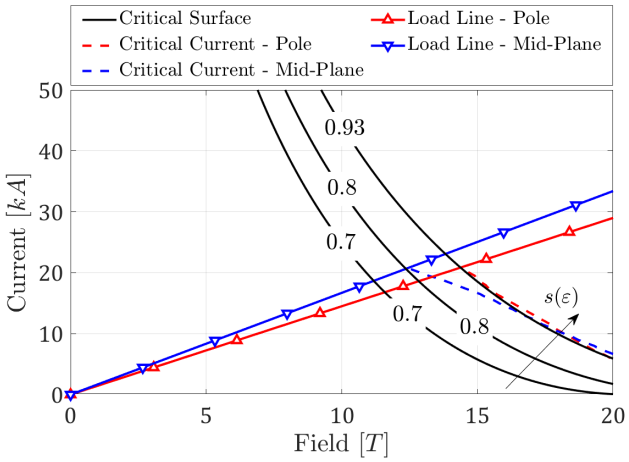

Fig. 12. Load line as computed from the strand model. The pole and mid-plane lines refer to the strands highlighted in Fig. 11. T = 1.9 K.

reality, this assumption is not verified, as there is no data for strand or cables under radial loads, but only under transversal and longitudinal loads. Therefore, at the present moment we are constrained to consider these directions as equivalent. Eventual future (numerical or experimental) studies might provide further information that would allow to validate the model also in this direction. It will then important to rotate not only the cables but also the strand coordinate system with a similar approach to the one described in Appendix A.

B. Critical Current

The critical current can be computed from the strain components of Fig. 8 and the magnetic field from Fig. 4, using Eq. 13. In practice, no operation is possible for the magnet unless the critical current is higher than the powering current in all the strands. An hypothetical limit on each strand was computed ramping the current and computing the critical field or current on each strand. If the current and field would meet the critical surface reduced by the mechanical strains at any point, that condition was stored and marked as critical current for that strand. The resulting critical current for each strand is shown in Fig. 11. The graph also provides the ideal critical current at the same magnet current, when considering the actual short sample limit (strain function equal to 0.93). Two locations are highlighted: a strand on the pole turn, and the inner strand on the mid-plane turn. The former corresponds to the peak field location, and the latter to the location of the minimum critical current. The critical current on the pole strand is equal to the short sample limit of 21.2 kA, the same value found when neglecting the strains acting on the conductor. This is partially expected, as the pole turn is completely detached from the winding pole, with no remaining prestress on it. On the other hand, it is worth to notice that this means that the effect of the residual plastic strain in copper regions is negligible.

For any MQXF magnet experiencing this loss of prestress, the critical current at the winding pole strand would be the same (21.2 kA), while the mid-plane strand would instead see a limiting current of 23.1 kA. The critical current reduction on the midplane is therefore equal to 2 kA. A smaller amount of reduction is instead apparent on the few strands near the corner of the pole block of the outer layer. This corner is creating an intensification of the stresses, which result in this current reduction. It is worth to notice that at this level some amount of permanent degradation might appear, further reducing the available critical current on the mid-plane.

C. Critical Field

The critical current as a function of the local magnetic field is shown in Fig. 12 for the two strands indicated by arrows in Fig. 11. The plot also provides the load line for these strands (critical current as function of the magnetic field), and 3 black lines representing slices of the critical surface at 1.9 K and with a strain function of 0.93, 0.8, and 0.7. The plot shows that the pole strand does not experience any critical current reduction, and its critical current follows closely the line corresponding to a strain function of 0.93, the same value needed to match the behavior of the short samples. The mid-plane strand sees instead a progressive amount of critical current reduction as the magnet current is increased. The mid-plane load line meets the critical surface at a current of 21.1 kA, and with a strain function equal to 0.8.

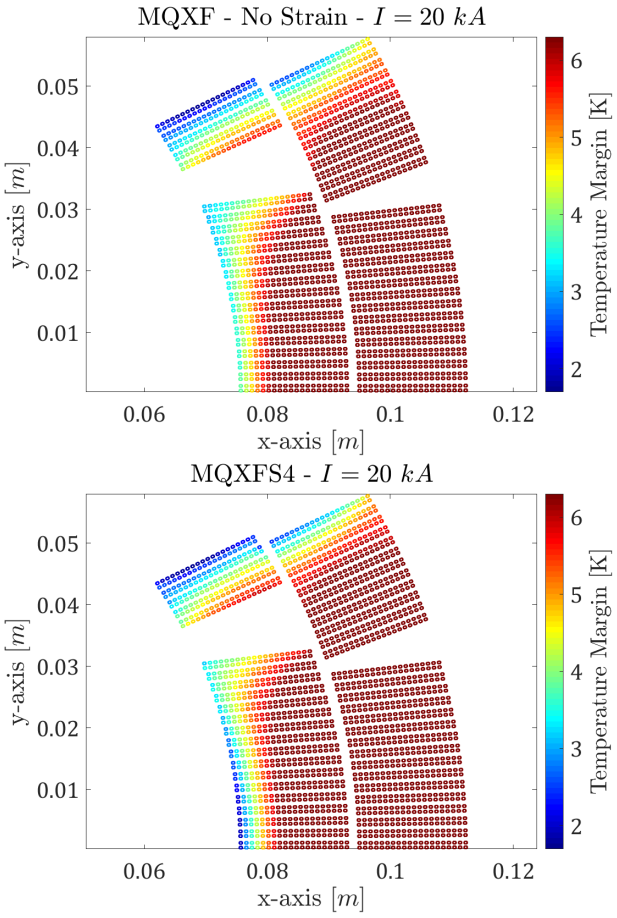

Fig. 13. Temperature margin at 20 kA with no strain applied (top), and with the strain (bottom). The reduction of the temperature margin is most evident on the inner radius of the mid-plane turns and at the inner layer pole block near the outer layer pole block corner.

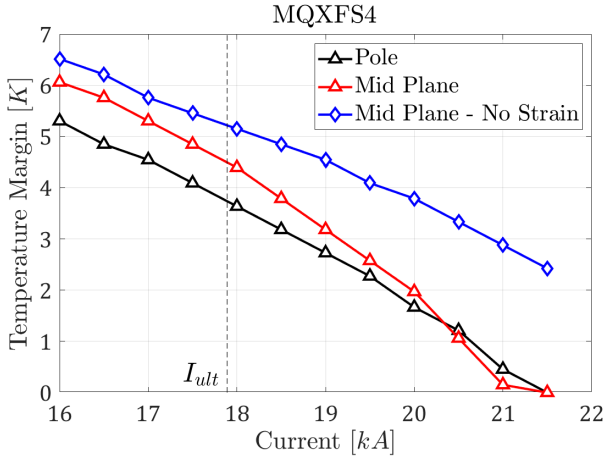

Fig. 14. Temperature margin as a function of the powering current on the pole, mid-plane and on the mid-plane with no applied strain. The reduction of the temperature margin at ultimate current ($I_{ult} = 17.89\ kA$) is 0.4 K.

D. Temperature Margin

Sudden disturbances occurring during the magnet operation can locally increase the temperature of the conductor. Depending on the available margin with respect to the critical surface, this can bring a conductor region above the critical temperature, restoring the normal state. This region can then potentially propagate, quenching the magnet. Three mechanism are generally considered as responsible for these energy releases: frictional heating due to wire motion; failure in the epoxy impregnation; microyielding in the conductor [44].

As the applied strain state moves the critical surface, the available temperature margin can be reduced. For a given current, field and strain function, the scaling law would allow to compute the temperature margin as $T_m = T_c - T_o$, where T_o is the operating temperature, 1.9 K, and T_c the critical temperature at a given current and field in the strand. In Fig. 13 the temperature margin at 20 kA is provided neglecting (top) considering (bottom) the effect of mechanical strains. The reduction of the temperature margin is evident in the lower strain function regions (see also Fig. 10): the inner radius of the mid-plane and the inner layer pole block second turn, near the corner of the outer layer pole block. The lower value of the strain function in this latter region might explain the limiting quenches that were identified as starting from one of the inner turns of the pole block in the magnet tests.

The temperature margin was also computed as a function of the powering current. Fig. 14 shows the variation of the margin on the mid-plane and pole. The plot also provides the same result when neglecting the mechanical strains on the mid-plane. As the results on the pole turn are equivalent when considering and neglecting the mechanical strains, only one set of results is shown for this location. The reduction of the temperature margin at ultimate current is 0.4 K, and increases gradually up to the maximum of 2.5 K at 21.0 kA. This means that, as we approach the short sample limit, sudden disturbances are more likely, or at least as likely, to generate a quench on the mid-plane region than in the pole turn.

VII. Coil Block Comparison

It might be of interest to run a simplified analysis of the magnet model during the early stages of the design. In this context, it is still very important to estimate the actual magnet performances, and in particular the critical current limit. The results from [12] were suggesting to limit the actual coil stress to about 200 MPa.

Here we can instead compare the critical current reduction obtained with the non-linear strand model to the stresses from a reference linear elastic homogenized model. Fig. 15 provides the azimuthal stress as computed in a MQXF FE model made with the traditional coil block strategy. The stress is equal to 130 MPa at ultimate current, and 175 MPa at 21 kA, the actual limiting current of the magnet for the computations of Section VI. At ultimate current the strand model was instead providing an average strand peak stress of 205 MPa on the Nb_3Sn region (Fig. 9). While it is not possible to use a one to one translation from the non-linear strand model to this linear elastic homogenized model, it is still interesting to underline that the limit current occurs for a stress of 175 MPa, which is close to the 200 MPa value detected from past experiments as limiting [12]. It is however important to keep in mind that in reality there is no direct equivalence

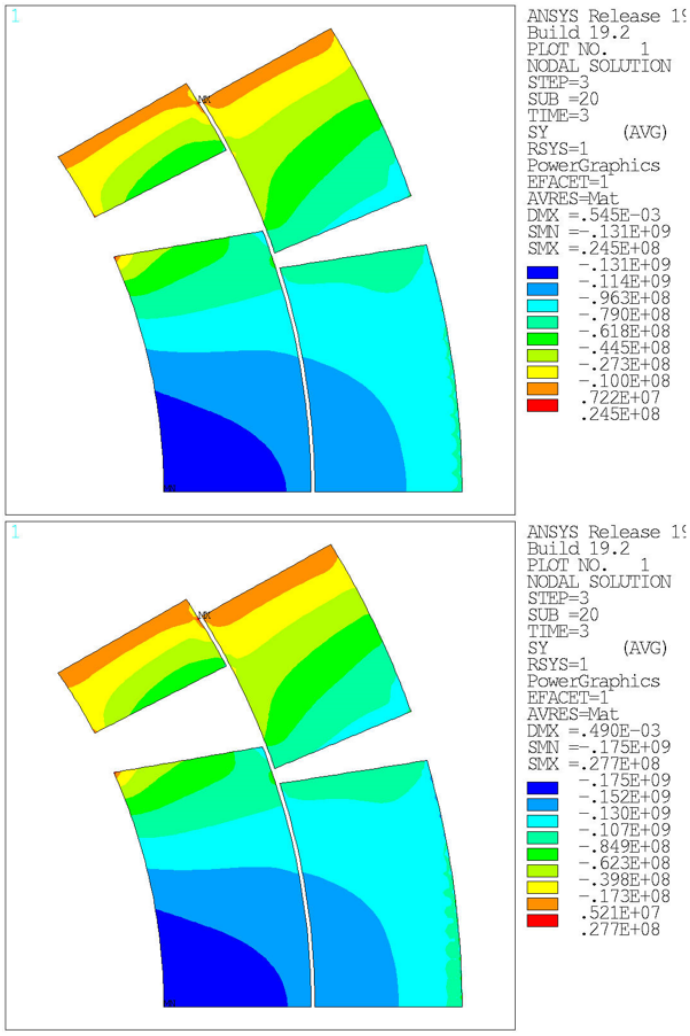

Fig. 15. Azimuthal stress, in Pa, as computed with a linear elastic homogenized model at ultimate current (top), and at 21 kA (bottom).

between the strain function and the stress state, especially when considering the of the strands. For example, because of Rutherford cables anisotropy and the impact of plastic strains in the copper regions, this number might change as a function of the load direction or history. Finally, the slope of the load line on severely strained strands plays an important role: two different magnet designs might see a similar maximum stress but different load lines on the most stressed strands. Trivially, the impact of high stresses on the magnet performances will be lower in the low field regions of the windings.

VIII. Conclusion

A methodology was developed to study the effect of strains, in the reversible region, on the critical current of superconducting magnets. The methodology is based on the laws developed on longitudinally loaded superconducting strands, and a number of experiments that allowed to validate the intermediate steps.

The core of the methodology there is a coil modeling strategy that allows to obtain the strains on the Nb_3Sn regions of the strands, and another strategy to use the strain function to compute the critical current reduction on those regions. The methodology was validated in the past by comparing numerical results with stiffness and critical current reduction data taken on cable stacks.

The relative simplicity and low computational cost of this approach allows the application also to 2D magnet models. The coil modeling strategy used allowed to match very well the measured mechanical behavior of the magnet, with no calibration. A remarkable agreement was found during all the phases of the magnet life: room temperature preload, cool-down and powering. Therefore, it could be an important tool for future magnet designs, in particular in those situations where a new cable design is being developed and 10 stacks measurements are still not available.

The critical current computation showed that, for the MQXF magnet, the actual critical current limit is on the mid-plane and not on the pole. Results also showed potential critical regions in the magnet (e.g. pole corners). The motion of the critical surface due to the applied strain also reduced the available temperature margin on the mid-plane and on near the pole. This might be one of the reasons why the limiting quenches on all the short models were not on the pole turn but in the inner turns.

The comparison with coil block FE models allowed to confirm the empirically evaluated limit values for the stress, suggesting that to avoid the reversible critical current reduction is necessary to keep the stress in the coil below 175 MPa.

Acknowledgments

This work was supported by the Director, Office of Science, High Energy Physics, and U.S. Department of Energy under contract No. DE-AC02-05CH11231.

The authors wish to thank S. Izquierdo Bermudez, I. Pong and S. Stoyonev for all the useful suggestions.

ANSYS and MATLAB code to facilitate the future usage of this methodology is available at: *https://github.com/giorgiovallone/Nb3Sn*.

Appendix
Cable positioning in the FE model

Fig. 16 shows an hypotetical cable inside of a coil block. The position of the cable is defined by the coordinates (x_c, y_c) of the cable center P_c and the rotation of the cable α_i. The four edges of the coil block are A, B, C and D. In a cylindrical coordinate system with origin in O, we can indicate with (r_A, θ_A) the coordinates of the edge A and similarly the ones of the other edges.

The inclination of the edge going from A to B, α_{c0}, can be computed from their horizontal and vertical distance, dx_{AB} and dy_{AB}, as:

$$dx_{AB} = (r_o \cos(\theta_b) - r_i \cos(\theta_a))/2 \quad (14)$$

$$dy_{AB} = (r_o \sin(\theta_b) - r_i \sin(\theta_a))/2 \quad (15)$$

$$\alpha_{c0} = \arctan(dy_{AB}/dx_{AB}) \quad (16)$$

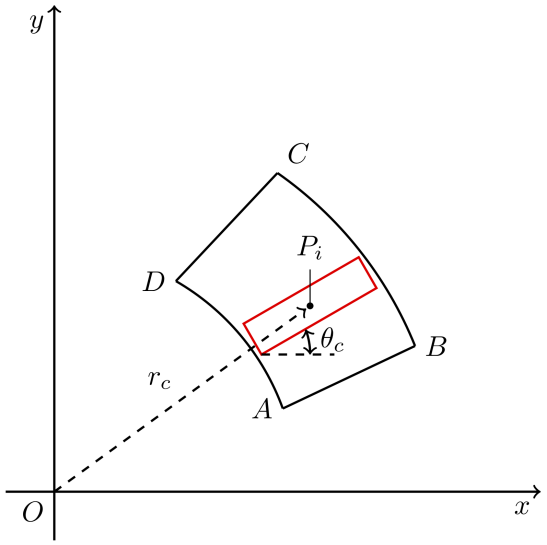

Fig. 16. Sketch of a Rutherford cable positioned inside a coil block.

If the number of cables in the block is N_c, we can compute the relative angle between cables α_C as:

$$dx_{CD} = (r_o \cos(\theta_c) - r_i \cos(\theta_d))/2 \quad (17)$$

$$dy_{CD} = (r_o \sin(\theta_c) - r_i \sin(\theta_d))/2 \quad (18)$$

$$\alpha_c = (\arctan(y_{px}/x_{px}) - \alpha_{c0})/N_c \quad (19)$$

The rotation of the $i-th$ cable, counting from the bottom to the top, α_i is then:

$$\alpha_i = \alpha_c(i - 1/2) + \alpha_{c0} \quad (20)$$

If we assume that the i-th cable center P_i will be at a radius r_c equal to the average of the inner and outer radius of the block (r_i and r_o), we can obtain the centroid cartesian coordinates as:

$$x_c = r_c \cos(\alpha_p(i - 1/2) + \alpha_{p0}) \quad (21)$$

$$y_c = r_c \sin(\alpha_p(i - 1/2) + \alpha_{p0}) \quad (22)$$

where α_{p0} and α_p are defined as:

$$x_{px} = (r_o \cos(\theta_b) - r_i \cos(\theta_a))/2 + r_i \cos(\theta_a) \quad (23)$$

$$y_{px} = (r_o \sin(\theta_b) - r_i \sin(\theta_a))/2 + r_i \sin(\theta_a) \quad (24)$$

$$\alpha_{p0} = \arctan(y_{px}/x_{px}) \quad (25)$$

$$x_{px} = (r_o \cos(\theta_c) - r_i \cos(\theta_d))/2 + r_i \cos(\theta_d) \quad (26)$$

$$y_{px} = (r_o \sin(\theta_c) - r_i \sin(\theta_d))/2 + r_i \sin(\theta_d) \quad (27)$$

$$\alpha_p = (\arctan(y_{px}/x_{px}) - \alpha_{p0})/N_c \quad (28)$$

REFERENCES

[1] L. Bottura and B. Bordini, "Jc(B, T, e) parameterization for the ITER Nb_3Sn production," *Ieee Transactions on Applied Superconductivity*, vol. 19, no. 3, pp. 1521–1524, 2009.

[2] P. Ferracin *et al.*, "Development of MQXF: The Nb_3Sn low-β quadrupole for the HiLumi LHC," *IEEE Transactions on Applied Superconductivity*, vol. 26, no. 4, pp. 1–7, 2016.

[3] J. Ekin, "Strain scaling law for flux pinning in practical superconductors. part 1: Basic relationship and application to Nb_3Sn conductors," *Cryogenics*, vol. 20, no. 11, pp. 611–624, 1980.

[4] ——, "Effect of transverse compressive stress on the critical current and upper critical field of Nb_3Sn," *Journal of Applied Physics*, vol. 62, no. 12, pp. 4829–4834, 1987.

[5] H. H. J. ten Kate, H. W. Weijers, and J. M. van Oort, "Critical current degradation in Nb_3Sn cables under transverse pressure," *IEEE Transactions on Applied Superconductivity*, vol. 3, no. 1, pp. 1334–1337, 1993.

[6] E. Barzi *et al.*, "Strand critical current degradation in Nb_3Sn rutherford cables," *IEEE Transactions on Applied Superconductivity*, vol. 11, no. 1, pp. 2134–2137, 2001.

[7] A. Godeke, *Performance boundaries in Nb_3Sn superconductors*. 2005.

[8] L. F. Goodrich *et al.*, "Method for determining the irreversible strain limit of Nb_3Sn wires," *Superconductor Science and Technology*, vol. 24, no. 7, p. 075 022, 2011.

[9] B. Bordini, P. Alknes, L. Bottura, L. Rossi, and D. Valentinis, "An exponential scaling law for the strain dependence of the Nb_3Sn critical current density," *Superconductor Science and Technology*, vol. 26, no. 7, p. 075 014, 2013.

[10] H. Oguro *et al.*, "Room and low temperature direct three-dimensional-strain measurements by neutron diffraction on as-reacted and prebent CuNb / Nb_3Sn wire," *Journal of applied physics*, vol. 101, no. 10, p. 103 913, 2007.

[11] P. Ebermann *et al.*, "Irreversible degradation of Nb_3Sn Rutherford cables due to transverse compressive stress at room temperature," *Superconductor Science and Technology*, vol. 31, no. 6, p. 065 009, 2018.

[12] H. Felice *et al.*, "Performance of a Nb_3Sn quadrupole under high stress," vol. 21, no. 3, pp. 1849–1853, 2011.

[13] D. Tommasini *et al.*, "The 16 T dipole development program for FCC," *IEEE Transactions on Applied Superconductivity*, vol. 27, no. 4, pp. 1–5, 2017.

[14] S. Caspi *et al.*, "Measured strain in Nb_3Sn coils during excitation and quench," *IEEE Transactions on Applied Superconductivity*, vol. 15, no. 2 PART II, pp. 1461–1464, 2005.

[15] S. Caspi and P. Ferracin, "Toward integrated design and modeling of high field accelerator magnets," *IEEE Transactions on Applied Superconductivity*, vol. 16, no. 2, pp. 1298–1303, 2006.

[16] C. Löffler, M. Daly, E. Nilsson, and F. Savary, "Finite element analysis of the mechanical conditions of the Nb_3Sn cable of the 11 T dipole magnet during operation," *IEEE Transactions on Applied Superconductivity*, vol. 28, no. 4, pp. 1–5, 2018.

[17] M. Daly *et al.*, "Multiscale approach to the mechanical behavior of epoxy impregnated Nb_3Sn coils for the 11 T dipole," *IEEE Transactions on Applied Superconductivity*, vol. 28, no. 3, pp. 1–6, 2018.

[18] E. Barzi, C. Franceschelli, I. Novitski, F. Sartori, and A. V. Zlobin, "Measurements and modeling of mechanical properties of Nb_3Sn strands, cables, and coils," *IEEE Transactions on Applied Superconductivity*, vol. 29, no. 5, pp. 1–8, 2019.

[19] R. Hoard and R.W., "Effects of strain on the superconducting properties of Niobium-Tin conductors," Lawrence Livermore National Laboratory (LLNL), Livermore, CA (United States), Tech. Rep., 1980.

[20] B. ten Haken, A. Godeke, and H. H. J. ten Kate, "The strain dependence of the critical properties of Nb_3Sn conductors,"

Journal of Applied Physics, vol. 85, no. 6, pp. 3247–3253, 1999.

[21] W. Markiewicz, "Elastic stiffness model for the critical temperature Tc of Nb_3Sn including strain dependence," *Cryogenics*, vol. 44, no. 11, pp. 767–782, 2004.

[22] S. Murase and H. Okamoto, "FEM analysis of three directional strain states under applied tensile stress for various composite superconductors," *IEEE Transactions on Appiled Superconductivity*, vol. 14, no. 2, pp. 1130–1133, 2004.

[23] T. Wang, L. Chiesa, M. Takayasu, and B. Bordini, "A novel modeling to predict the critical current behavior of Nb_3Sn PIT strand under transverse load based on a scaling law and finite element analysis," *Cryogenics*, vol. 63, pp. 275–281, 2014.

[24] G. Vallone, B. Bordini, and P. Ferracin, "Computation of the reversible critical current degradation in Nb_3Sn Rutherford cables for particle accelerator magnets," *IEEE Transactions on Applied Superconductivity*, 2018.

[25] B. Bordini *et al.*, "Conceptual design of a new sample holder for the FRESCA cable test station," *IEEE Transactions on Applied Superconductivity*, vol. 20, no. 3, pp. 1511–1514, 2010.

[26] B. Bordini, P. Alknes, A. Ballarino, L. Bottura, and L. Oberli, "Critical current measurements of high-Jc Nb_3Sn Rutherford cables under transverse compression," *IEEE Transactions on Applied Superconductivity*, vol. 24, no. 3, pp. 1–5, 2014.

[27] J. Duvauchelle, B. Bordini, J. Fleiter, and A. Ballarino, "Critical current measurements under transverse pressure of a Nb_3Sn Rutherford cable based on 1 mm RRP wires," *IEEE Transactions on Applied Superconductivity*, vol. 28, no. 4, pp. 1–5, 2018.

[28] D. R. Dietderich, R. M. Scanlan, R. P. Walsh, and J. R. Miller, "Critical current of superconducting Rutherford cable in high magnetic fields with transverse pressure," *IEEE Transactions on Applied Superconductivity*, vol. 9, no. 2, pp. 122–125, 1999.

[29] K.-H. Mess, S. Wolff, *et al.*, *Superconducting accelerator magnets*. World Scientific, 1996.

[30] L. Rossi and O. Brüning, "High Luminosity Large Hadron Collider a description for the european strategy preparatory group," no. 284404, 2012.

[31] S. Caspi *et al.*, "The use of pressurized bladders for stress control of superconducting magnets," *IEEE Transactions on Applied Superconductivity*, vol. 11, no. 1 II, pp. 2272–2275, 2001.

[32] M. Juchno *et al.*, "Mechanical Qualification of the Support Structure for MQXF, the Nb_3Sn Low-β quadrupole for the high luminosity LHC," *IEEE Transactions on Applied Superconductivity*, vol. 26, no. 4, 2016.

[33] G. Vallone *et al.*, "Mechanical performance of short models for MQXF, the Nb_3Sn low-β quadrupole for the Hi-Lumi LHC," *IEEE Transactions on Applied Superconductivity*, pp. 1–1, 2016.

[34] G. Vallone and P. Ferracin, "Modeling coil-pole debonding in Nb_3Sn superconducting magnets for particle accelerators," *IEEE Transactions on Applied Superconductivity*, 2017.

[35] G. Vallone *et al.*, "Mechanical analysis of the short model magnets for the Nb_3Sn quadrupole MQXF," *IEEE Transactions on Applied Superconductivity*, vol. 28, no. 3, pp. 1–6, 2018.

[36] G. Vallone *et al.*, "Summary of the mechanical performances of the 1.5 m long models of the Nb_3Sn low-β quadrupole MQXF," *IEEE Transactions on Applied Superconductivity*, 2019.

[37] H. Bajas *et al.*, "Test results of the short models MQXFS3 and MQXFS5 for the HL-LHC upgrade," *IEEE Transactions on Applied Superconductivity*, 2017.

[38] S. Stoynev *et al.*, "Summary of test results of MQXFS1 - the first short model 150 mm aperture Nb_3Sn quadrupole for the high-luminosity LHC upgrade," *IEEE Transactions on Applied Superconductivity*, 2017.

[39] F. Mangiarotti *et al.*, "Test results of the CERN HL-LHC low-β quadrupole short models MQXFS3c and MQXFS4," *IEEE Transactions on Applied Superconductivity*, 2019.

[40] S. Stoynev *et al.*, "Summary of test results of MQXFS1 - the first short model 150 mm aperture Nb_3Sn quadrupole for the High-Luminosity LHC upgrade," *IEEE Transactions on Applied Superconductivity*, vol. 28, no. 3, pp. 1–5, 2018.

[41] R. Meuser, S. Caspi, and W. Gilbert, "Measured mechanical properties of superconducting coil materials and their influence on coil prestress," *IEEE Transactions on Magnetics*, vol. 17, no. 5, pp. 2320–2323, 1981.

[42] K. Couturier, P. Ferracin, W. Scandale, E. Todesco, and D. Tommasini, "Thermomechanical properties of the coil of the superconducting magnets for the Large Hadron Collider," *IEEE Transactions on Applied Superconductivity*, vol. 12, no. 2, 2002.

[43] H. Felice *et al.*, "Test results of TQS03: A LARP shell-based Nb_3Sn quadrupole using 108/127 conductor," *Journal of Physics: Conference Series*, vol. 234, no. 3, p. 032 010, 2010.

[44] A. Devred, "Quench origins," in *AIP*, vol. 1262, 1992, pp. 1262–1308.